nature nanotechnology

Article

https://doi.org/10.1038/s41565-024-01763-6

Local control of polarization and geometric phase in thermal metasurfaces

Received: 24 April 2024

Accepted: 17 July 2024

Published online: 23 August 2024

Check for updates

J. Ryan Nolen[1,3], Adam C. Overvig[1,3], Michele Cotrufo[1] & Andrea Alù[1,2]

Thermal emission from a hot body is inherently challenging to control due to its incoherent nature. Recent advances have shown that patterned surfaces can transform thermal emission into partially coherent beams with tailored directionality and frequency selectivity. Here we experimentally demonstrate polarization-selective, unidirectional and narrowband thermal emission using single-layer metasurfaces. By implementing polarization gradients across the surface, we unveil a generalization of the photonic Rashba effect from circular polarizations to any pair of orthogonal polarizations and apply it to thermal emission. Leveraging pointwise specification of arbitrary elliptical polarization, we implement a thermal geometric phase and leverage it to prove previous theoretical predictions that asymmetric chiral emission is possible without violating reciprocity. This general platform can be extended to other frequency regimes in efforts to compactify metasurface optics technologies without the need for external coherent sources.

Incandescence is a ubiquitous source of light, characterized by incoherent, broadband, uncollimated and unpolarized emission[1], features that often limit its applicability and broad appeal compared with coherent sources. Addressing these shortcomings may yield a broad range of cheap infrared (IR) sources with groundbreaking impact on various technologies[2]. Towards this goal, recent demonstrations have leveraged strongly coupled material resonances with surface waves to enhance the coherence of thermal emission, leading to narrowband, collimated and linearly polarized responses[3–14]. These structures typically rely on phonon polaritons, which are not necessarily compatible with integrated technologies and leave a large part of the mid-IR range inaccessible (including the 3–5 μm atmospheric transparency window). More fundamentally, surface-wave-mediated emission has so far been limited to simple, symmetric forms of wavefront shaping and to *p*-polarized waves[4].

In parallel, 'metasurfaces'—engineered thin films compatible with standard micro- and nanofabrication—offer a paradigm of compactification of optical systems. Typical metasurfaces are composed of building blocks affording local amplitude and phase control over externally impinging coherent light. By spatially varying these 'meta-units', a wide range of wavefront-shaping functionalities is enabled, including beam steering, focusing and vortex beam generation. However, unlike polariton-mediated emitters, wavefront-shaping metasurfaces are not designed to correlate the light across their aperture. Instead, they rely on the spatial coherence of the incoming light to meaningfully pattern the output waveform[15,16].

Recently, the fields of thermal emission and metasurfaces have been converging to enable careful engineering of the optical density of states, including chiral states. As a prominent example, the photonic Rashba effect involves spin-split bi-directional thermal emission of circular polarization (CP), wherein the spin of one handedness is associated with one direction while the spin of opposite handedness is associated with the opposite direction (also known as spin anti-symmetry). In materials, this is associated with a splitting of electronic spin bands, known as the Rashba effect[17]. In flat optics, spin splitting variously manifests as spin-momentum locking in topological photonics[18], spin-sorting in plasmonic devices[19], spin-dependent deflection in geometric phase metasurfaces[20], and emission in thermal[21], quantum[22] and perovskite[23] systems. Beyond these chiral responses limited to oblique angles of emission, symmetry-broken metasurfaces have recently demonstrated absorption[24,25], and (concurrently with this manuscript) emission[26,27], of CP states at normal incidence. However,

[1]Photonics Initiative, Advanced Science Research Center, City University of New York, New York, NY, USA. [2]Physics Program, Graduate Center of the City University of New York, New York, NY, USA. [3]These authors contributed equally: J. Ryan Nolen, Adam C. Overvig. e-mail: aalu@gc.cuny.edu

https://doi.org/10.1038/s41565-024-01763-6

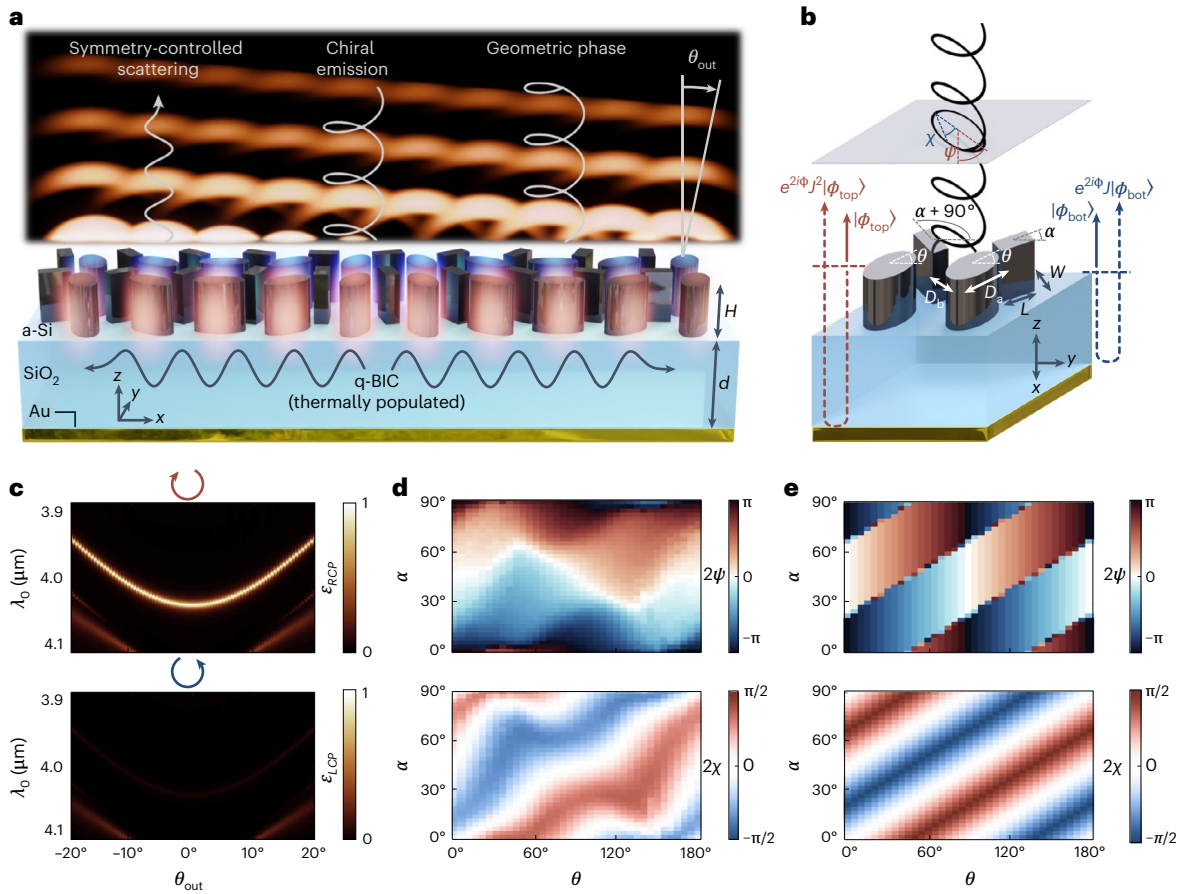

Fig. 1 | Design and functionality of a thermal metasurface. a, Schematic view of the approach in the work: a thermally populated q-BIC emits to free space via symmetry-controlled scattering, including chiral emission with a tunable geometric phase that may be spatially graded to tilt the output angle of the wave, θ_{out}. **b**, Geometry of a meta-unit cell, with depictions of the scattered components from the top and bottom interfaces of the silicon layer. By controlling the Jones matrix J and the linear polarization states $|\phi_{top,bottom}\rangle$, thermal emission of any ellipticity χ and orientation ψ may be achieved. **c**, Simulated RCP (top) and LCP (bottom) emission from an example meta-unit array, as a function of wavelength λ_0 and θ_{out}. **d**, Simulated polarization state as a function of θ and α, where 2ψ and 2χ are the longitude and latitude on the Poincaré sphere, respectively. **e**, Calculated polarization state using a TCMT based on the scattering model in **b**. Note that, by symmetry, the range is equivalent to the range but with a phase shift arising from a sign flip in the q-BIC scattering.

the use of lossy metallic structures has restricted the spatial and temporal coherence as well as manufacturing compatibility. Period-doubled dielectric metasurfaces have been shown to produce spatially and temporally coherent light emitting along the device normal but are limited to unpolarized and unpatterned beams[28].

Despite these successes, the generation of arbitrary IR frequencies with tailored spatial profiles of amplitude, phase and polarization still requires complex and bulky optical systems comprising cascaded stacks of optical devices. The compactification of broadly customizable thermal emission within a mature fabrication platform remains an outstanding challenge. Most basically, unidirectional (asymmetric) thermal emission of a chosen arbitrary polarization to a single half-space, and bidirectional control of polarizations other than circular, have not been demonstrated in a single metasurface. Underpinning this challenge is that any such asymmetry in the thermal emission pattern—of any magnitude—appears to violate reciprocity, rendering them impossible without magnetic, nonlinear or time-varying materials[29]. In contrast to this appearance, a recent theoretical proposal clarified that 'thermal metasurfaces'[30] may support such asymmetric emission patterns in reciprocal structures by combining conventional metasurface designs with emerging advances in engineered non-localities[31–36]. This feat requires correlating the emission across the surface, while simultaneously shaping it pointwise. The theoretical design proposed in ref. 30 involved multi-layered nanofabrication with careful alignment, presenting major barriers to their experimental realization and proof of these claims. A single-layer monolithic implementation of thermal metasurfaces with advanced functionality and compatibility with standard, low-loss dielectric material platforms remains a key unsolved obstacle. Experimental observation of arbitrary directional or polarization asymmetry remains elusive in any platform that obeys reciprocity.

Here, we introduce a thermal metasurface platform that fills this need, experimentally achieving enhanced spatial and temporal coherence along with pointwise control over the emitted phase or polarization state. We show arbitrarily polarized emission in thermal metasurfaces composed of a single patterned layer and material systems compatible with standard fabrication methods. Our platform is not limited to the polariton resonance frequency or by the losses of plasmonic systems; here, we address the 3–5 μm atmospheric transparency window as a notable example. We further show that, by varying the polarization state across the device, bi-directional emission to any set of orthogonal polarizations is achievable. This generalizes the photonic Rashba effect beyond spin states, signifying that past observations and device functionalities are a subset of a broader phenomenon. Finally, we reveal a thermal geometric phase achieved by tuning from a bound state condition to a degenerate critically coupled condition. Using this concept, we demonstrate spin-selective unidirectional emission to a single half-space—the basic building block for thermal metasurfaces with custom wavefronts. In direct contrast to the photonic Rashba

https://doi.org/10.1038/s41565-024-01763-6

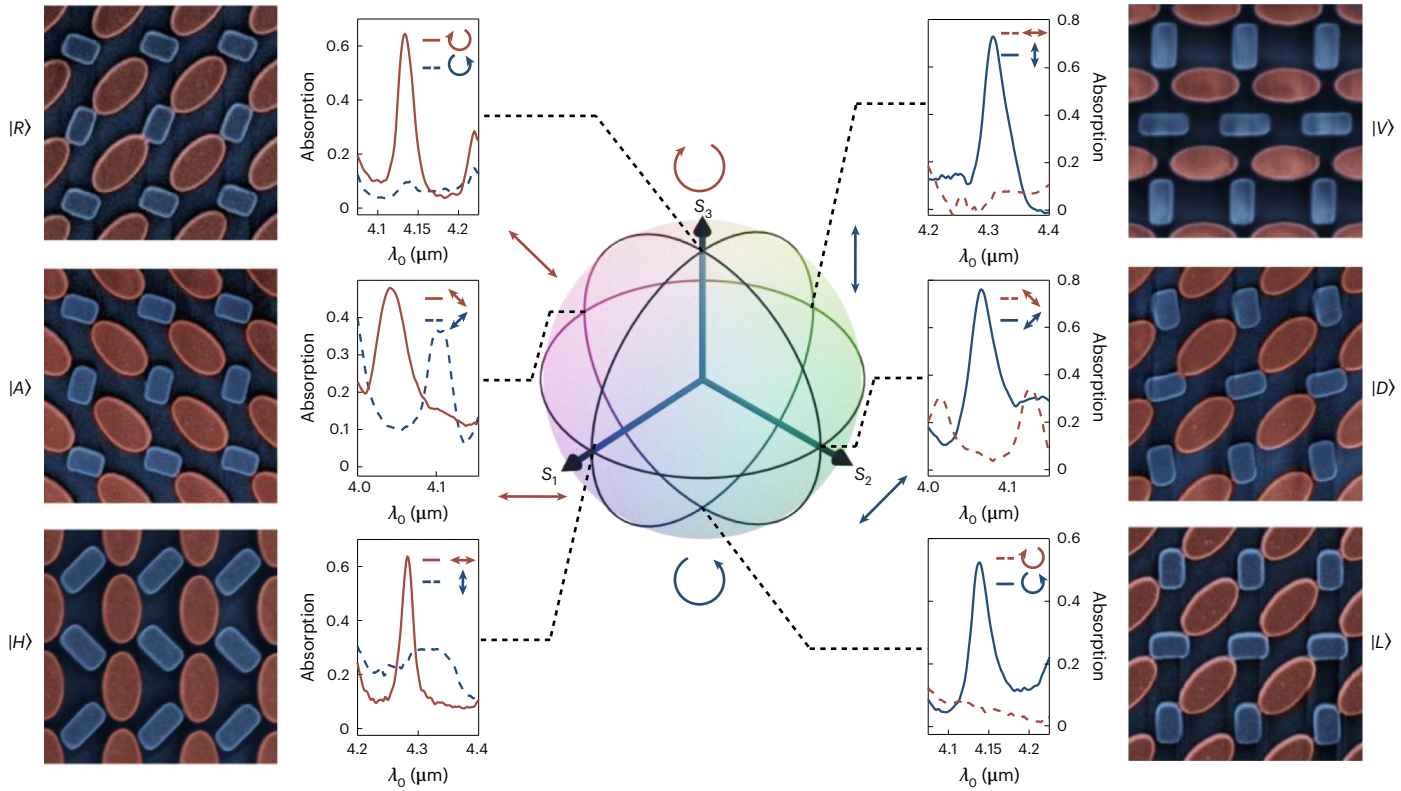

Fig. 2 | Experimental demonstration of polarization control. Counterclockwise from the top left: measured polarization-resolved spectra from six metasurfaces designed for RCP-, antidiagonal-, *x*-, LCP-, diagonal- and *y*-polarized emission. Insets show SEM images of the corresponding fabricated metasurfaces, with local elements shaded red and non-local elements shaded blue.

effect (spin anti-symmetry), this device experimentally demonstrates that reciprocal systems may control a single spin at will, without the presence of the opposite spin (spin asymmetry). Remarkably, our findings show that this intrinsically chiral response does not require multi-layer device architectures or oblique etching techniques[37]. We confirm these concepts through spatio-temporal coupled mode theory (STCMT)[38], numerical simulations and experimental characterization of our devices.

Metasurface design

We realized several thermal metasurfaces composed of amorphous silicon (a-Si) pillars atop silicon dioxide and gold films, whose scattering properties are locally controlled with symmetry-breaking design concepts to emit to arbitrary polarizations, including chiral emission with a geometric phase (Fig. 1a). The meta-units are carefully designed to control the absorption/emission by tuning the non-local scattering from the interfaces of the a-Si layer (Fig. 1b). This design is based on the implementation of a thermally populated quasi-bound state in the continuum (q-BIC)[39] supported by a periodic array of pillars, whose in-plane long-range order provides coherence to the thermal emission[3], including the production of narrowband, directional CP thermal emission (Fig. 1c) near a wavelength of 4 μm. The emission can be tuned throughout the mid-IR through a simple scaling of the geometric parameters (Supplementary Section 1). By careful design of the unit cell, full coverage over the entire Poincaré sphere is possible along the device normal (Fig. 1d,e). We stress that, while recent efforts have shown circularly polarized emission[26,27], here we report a single platform capable of exhibiting thermal emission with arbitrary elliptical polarization specified pointwise and with respect to the lattice of the device.

The meta-units comprise four micropillars: two identical local pillars (elliptical) oriented at an angle θ, controlling the local phase, and two non-local pillars (rectangular) oriented at angles α and $\alpha + 90°$, controlling the extended q-BIC mode. The angles θ and α are defined as the counterclockwise in-plane angles between the elongated direction of the corresponding pillar and the *y* axis. The rectangular bars lie at the interstitial sites of the elliptical array, as shown in Fig. 1b. The local pillars' major and minor diameters, D_a and D_b, are tuned to ensure a birefringent response, conferring a linear control over the geometric phase via the parameter θ (ref. 16). In contrast to conventional geometric phase metasurfaces, these pillars at the same time support a transverse magnetic q-BIC for any value of θ. When the length L and width W of the non-local pillars are equal, this state is symmetry protected, being bound to the surface and, hence, emitting no thermal radiation. As the symmetry in the non-local pillars is broken by making L and W unequal, the bound state becomes a q-BIC, and leaks to free space with a radiative Q-factor $Q \propto (L - W)^{-2}$ (ref. 40). These parameters are tuned such that the radiative and non-radiative Q-factors are identical across the entire device, a critical coupling condition that enables blackbody thermal emissivity with a linewidth customizable by tuning both the amount of material loss and the perturbation strength[40].

We control the scattering by the non-local pillars following selection rules that govern the excitation of q-BICs, which in vertically invariant (extruded) structures are limited to linear polarizations generated at both the top and bottom interfaces of the silicon pillars[33]. While previous theoretical work achieved chiral q-BICs by manipulating the two interfaces independently[35,36], or by introducing the non-local pillars only at the bottom interface[30], here we rely on a single-layer geometry to facilitate the fabrication and experimental demonstration. To overcome this challenge, we engineer the silicon thin film's average refractive index and the silicon dioxide thin film's thickness to largely suppress the scattering off the bottom interface via destructive interference. Consequently, the scattering from the top interface dominates the selection rules, and the emitted polarization state is the

https://doi.org/10.1038/s41565-024-01763-6

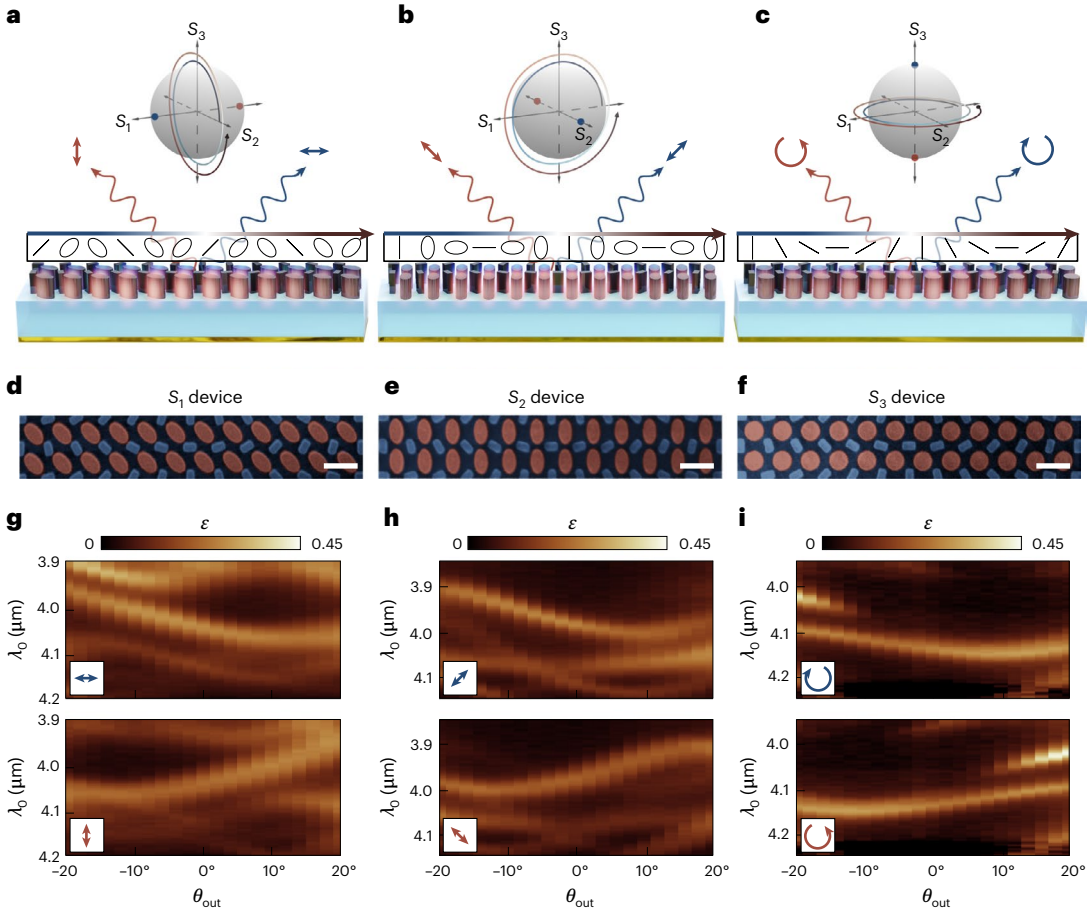

Fig. 3 | Generalized photonic Rashba effect. a, A thermal metasurface splitting *s* and *p* polarizations ($|V\rangle$ and $|H\rangle$) via a polarization gradient following the great circle on the Poincaré sphere in the S_2, S_3 plane. **b**, Thermal metasurface splitting $|A\rangle$ and $|D\rangle$ via a polarization gradient in the S_1, S_3 plane. **c**, Conventional spin-split dispersion, splitting $|L\rangle$ and $|R\rangle$ via a polarization gradient in the S_1, S_2 plane. The coloured arrows in **a**–**c** track the mapping of the polarization gradient's trajectory on the Poincaré sphere to the in-plane position along the devices. **d**–**f**, SEM of the fabricated S_1, S_2 and S_3 devices, respectively. Scale bars, 2 μm. **g**–**i**, Measured, polarization-resolved thermal emission of the fabricated S_1, S_2 and S_3 devices, respectively, showing generalized band splitting.

superposition of (1) the directly scattered linear polarization $|\phi_{top}\rangle$, with an angle following roughly 2α, emitting upwards without interacting with the rest of the metasurface, and (2) the indirectly scattered state that emits upwards after two passes through the metasurface (Fig. 1b). This latter component has the form $e^{2i\Phi}J^2|\phi_{top}\rangle$, where J is the Jones matrix of a single pass through the metasurface (controlled by the local pillars) and Φ is the propagation phase through the oxide slab. By choosing θ and α such that the direct and indirect scattering components from the top interface are orthogonal, CP emission is possible (Fig. 1c). More generally, any elliptical state is accessible by varying these parameters (Fig. 1d). To confirm the scattering model, we develop a temporal coupled mode theory (TCMT) (Supplementary Section 2) and compute the emitted polarization state as a function of θ and α (Fig. 1e), agreeing well with the full wave simulations.

Polarization control of thermal emission and the generalized photonic Rashba effect

Six fabricated metasurfaces (Fig. 2) were designed to absorb and thermally emit extremal values on the Poincaré sphere: horizontal and vertical polarization ($|H\rangle$ and $|V\rangle$), diagonal and antidiagonal ($|D\rangle$ and $|A\rangle$) and right-handed circularly polarized (RCP) and left-handed circularly polarized (LCP) ($|R\rangle$ and $|L\rangle$). We show in the figure their polarization-dependent absorption features, which due to time reversal validate their polarization-selective thermal emission, confirming the ability of single-layer dielectric metasurfaces to produce narrowband emission/absorption of custom polarization. This capability to arbitrarily specify the emitted polarization state enables the construction of lattices in which the local polarization state varies across the device aperture.

To showcase the pointwise control over polarization, we fabricated three devices incorporating distinct polarization gradients (Fig. 3). By splitting distinct Stokes parameters (defined by a Stokes vector $\mathbf{S} = [S_0, S_1, S_2, S_3]$), these devices collectively show representative examples of complete control over bidirectional emission of orthogonal polarizations. In each case, the gradient follows the trajectory of a great circle on the Poincaré sphere. The first device, dubbed the 'S_1 device' (Fig. 3a), follows the great circle intersecting the plane perpendicular to the S_1 axis. Therefore, the S_1 device splits S_1, with *s* polarization emitted towards the left and *p* polarization emitted to the right of the surface normal. Analogously, the 'S_2 device' (Fig. 3b) splits diagonal and anti-diagonal light via a polarization gradient perpendicular to the S_2 axis. Finally, the 'S_3 device' implements the conventional Rashba effect for thermal light, splitting left- and right-hand CP emission by maintaining linear polarization across the device. In these devices, the theoretical emissivity peak for a given polarization is limited to 0.5 due to the splitting of the band towards left and right. Theoretical and numerical studies of these devices agree well with our experiments, as described in Supplementary Section 3; all the Stokes parameters are reported in Supplementary Section 4; the nature of coherence is discussed in Supplementary Section 5.

https://doi.org/10.1038/s41565-024-01763-6

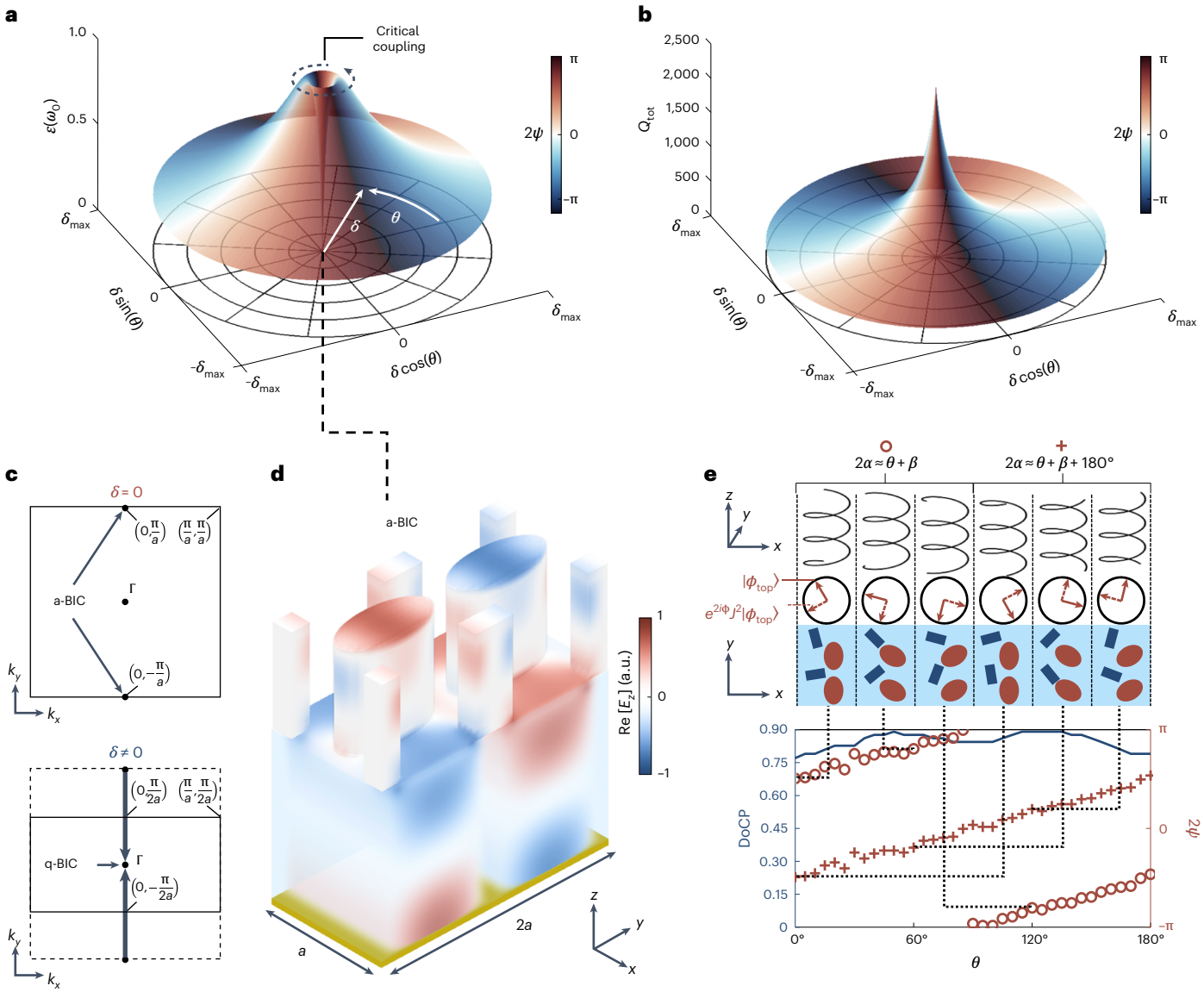

Fig. 4 | Thermal geometric phase: critical coupling near a topological feature. **a**,**b**, The resonant emissivity $\varepsilon(\omega_0)$ (**a**) and total Q-factor Q_{tot} (**b**) as a function of δ and θ computed by TCMT, where $\delta = L - W$. The colour map depicts the associated values of 2ψ for each set of parameters; the singularity at $\delta = 0$ has topological charge of 2 and confers a geometric phase to thermal emission with unity emissivity at a contour satisfying the critical coupling condition (dashed contour). **c**, Zone-folding scheme promoting an a-BIC into a q-BIC. **d**, Mode profile of the a-BIC computed by full-wave simulations when $\delta = 0$ and $\theta = 0$. **e**, Simulated DoCP and geometric phase Φ_{geo} (bottom) of a selected set of meta-units corresponding to the dashed contour in **a**, with example characteristic polarization helixes (top). Note that, while the local element is uniquely defined only on $\theta \in [0°, 180°)$, the non-local element is distinct by 90° on $\theta \in [180°, 360°)$, requiring the full 360° rotation of θ to define the entire contour.

Geometric phase for asymmetric and chiral thermal emission

Beyond polarization gradients, we next show that the local orientability of ψ confers a geometric phase to the thermal emission of CP states, born of critical coupling near a topological feature. To understand this feature, Fig. 4a,b shows the peak emissivity at resonance, $\varepsilon(\omega_0)$, and the total Q-factor $Q_{tot} = \left(Q_{rad}^{-1} + Q_{nr}^{-1}\right)^{-1}$ using TCMT. Here, the parameter space is in cylindrical coordinates, with the magnitude of the perturbation $\delta = L - W$ being the radius and θ being the angular coordinate (Q_{rad} is the radiative Q-factor and Q_{nr} is the non-radiative Q-factor, which we choose here to be $Q_{nr} = 2{,}500$). When $\delta = 0$, the non-local pillars are identical, and an additional translational symmetry is added to the unit cell. This renders the first Brillouin zone (FBZ) to be that of a square lattice (Fig. 4c, top), meaning the mode is bound (having $Q_{rad} = \infty$) in the 'artificial continuum' (a-BIC) associated with the periodicity $a \times 2a$ (Fig. 4d). When $\delta \neq 0$, the a-BIC is promoted to a q-BIC at the Γ point of the perturbed FBZ (Fig. 4c, bottom) with a geometric phase (see also refs. 36,41). The a-BIC results in the singularity seen in Fig. 4a,b, but deviating from this condition yields finite emission of CP states with an orientation 2ψ depending on θ. For a particular magnitude of perturbation, the critical coupling condition $\varepsilon(\omega_0) = 1$ can be achieved irrespective of θ. We then construct a library of meta-units using full-wave simulations to retrieve the emissivity and degree of circular polarization (DoCP; Fig. 4e) along the contour of unity emissivity (Fig. 4a, dashed curve), demonstrating the geometric phase associated with the local orientation of the local and non-local pillars. To maintain CP emission in the TCMT, we set $2\alpha = \theta + \beta$, with $\beta = 45° - \epsilon$ (with $\epsilon = 0.1$ chosen because the longitude 2ψ is undefined precisely at the poles), while in the full-wave simulations, the value of α is adjusted according to the maximal DoCP in Fig. 1d.

https://doi.org/10.1038/s41565-024-01763-6

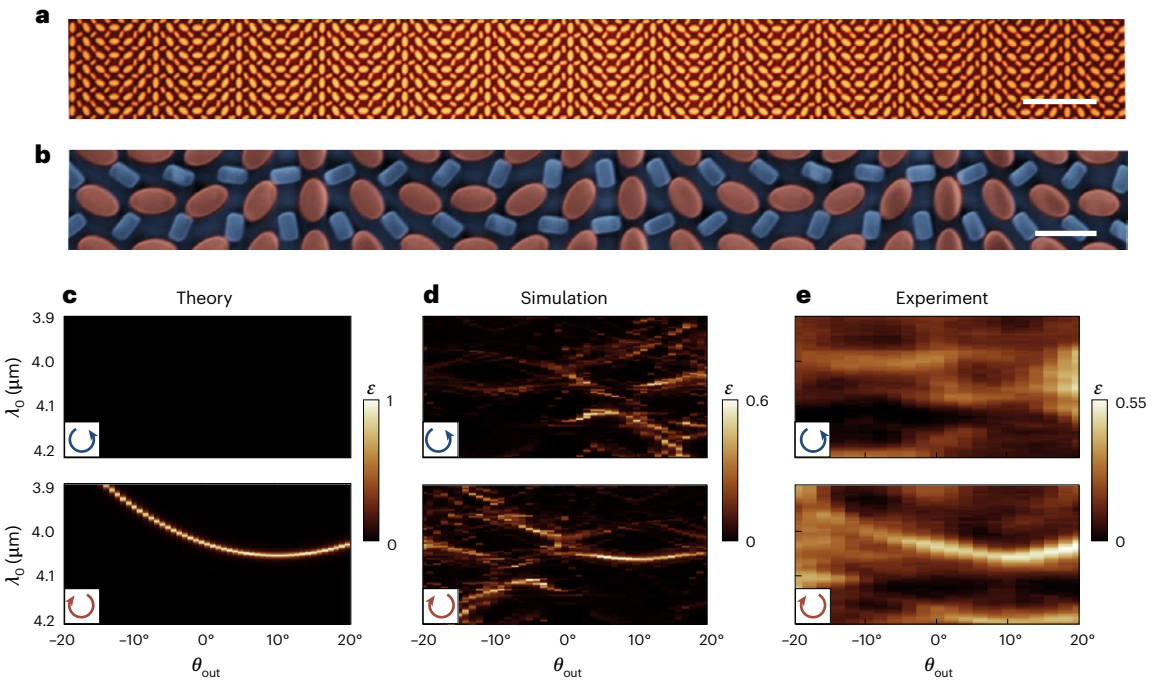

Fig. 5 | Spin-selective, unidirectional thermal emission. a,**b**, Optical (**a**) and SEM (**b**) images of a fabricated thermal metasurface. Scale bars, 10 μm (**a**) and 2 μm (**b**). **c**, Theoretical LCP (top) and RCP (bottom) emission as a function of outgoing angle θ_{out} and wavelength λ_0 from unidirectional thermal metasurfaces, computed using STCMT. **d**, Simulated LCP (top) and RCP (bottom) emission. **e**, Measured LCP (top) and RCP (bottom) emission, showing spin asymmetric thermal emission.

Next, we leverage this degree of freedom to experimentally demonstrate a gradient profile of the local phase applied to CP thermal emission. Figure 5a,b depicts optical and scanning electron microscopy (SEM) images of the fabricated sample, with an aperture of 4 × 3 mm in lateral dimensions. Figure 5c shows the spin-dependent dispersion calculated through STCMT (detailed in Supplementary Section 2)[38]. The response is similar to Fig. 1c but here is unidirectionally shifted in momentum. Next, we use numerical simulations of a realistic metasurface designed based on the library in Fig. 1e to demonstrate this phenomenon in a concrete geometry (Fig. 5d), where additional spectral features associated with other lattice modes emerge. Notably, the targeted q-BIC and these additional modes are not completely orthogonal, resulting in modal coupling that manifests itself as spectral splitting in the dispersion. Intriguingly, this effect degrades away from the band edge, narrowing the range of wavelengths and angles across which the response is highly efficient. In turn, this phenomenon interestingly suggests a mechanism for enhancing the control over spatial coherence[42]. Finally, Fig. 5e showcases the experimental confirmation of the metasurface functionality, clearly showing a momentum-shifted narrow band with a single spin state, avoiding substantial thermal emission of the opposite spin state to the opposite angle. These spin-selective, angle-resolved thermal emission measurements were performed at 300 °C using a setup detailed in Methods; the Stokes parameters of the devices are given in Supplementary Section 4; uncertainty analysis for the devices in Figs. 3 and 5 is also given in Methods. The measured Q-factor ($Q \approx 128$) is lower than for the simulated structure, and many unwanted additional spectral features are largely washed out. A broadband background emissivity $\varepsilon \approx 0.10$ is present (all data in Fig. 5e are greater than 0.10), but the targeted feature peaks at $\varepsilon \approx 0.55$, which is notably above the theoretical maximum of 0.5 in the conventional Rashba effect. The DoCP, defined as DOCP $= S_3/S_0$, is ~0.38, limited primarily by the background. Future optimizations may further reduce the background and improve the peak prominence compared with this proof-of-principle demonstration. Supplementary Section 6 provides a comparison with other approaches for thermal emission from flat optical devices. Supplementary Sections 7–9 discuss the dispersion, angle tunability and temperature dependence of phase gradient devices.

Conclusions

In this work, we have experimentally introduced a thermal metasurface platform extending our command of thermal emission beyond conventional paradigms. Despite the fundamentally incoherent nature of the underlying mechanism (incandescence), we have shown that suitably engineered structures leveraging both local and non-local optical scattering may corral the random fluctuations to emit into a far field channel of choice. We stress that our results are fully compatible with reciprocity, abiding the universal modal radiation laws[43]. Our reciprocal devices exhibit strong asymmetry in both polarization (beyond spin states) and direction. Moreover, in contrast to phonon-polariton approaches, our platform employs standard low-loss dielectrics structured via design principles rooted in symmetry; this approach is directly exportable to a wide range of optical frequencies and integrated platforms. We addressed the 3–5 μm atmospheric transparency window as a notable example. In contrast to plasmonic approaches, our platform is capable of highly coherent thermal emission via spatially extended modes, while achieving higher Q-factors (here between 100 and 200, compared with ~25 in plasmonic systems).

While our results provide proof of practice of a set of possibilities previously thought impossible without nonreciprocity, future efforts are bound to both improve on the performance and extend the functionalities shown herein. In the interest of establishing that *any* asymmetry is practically achievable, a number of simplifications were made in our implementations; as discussed in Supplementary Sections 10–12, there are clear pathways for improving the performance of thermal metasurfaces. Moreover, there are a number of extensions that may be made. In keeping with the vision of metasurfaces based on gradient building blocks, with careful design, our platform may employ these building blocks to produce focused emission, orbital angular momentum and custom vector beams tailored across two spatial dimensions.

Since our approach addresses the challenge of incoherence in the emission mechanism, we broadly expect this metasurface platform to be readily extended to systems with more inherent coherence, such as from luminescence[44,45] and fluorescence (for example, light-emitting diodes and two-dimensional materials), lasing, nonlinear and quantum media. Intriguingly, the asymmetries introduced here are possible without violating reciprocity, opening the possibility to incorporate our approach with non-reciprocal materials to violate Kirchhoff's laws[46] in previously unobtainable ways. Finally, given that our thermally emitted beams carry a net transverse and spin momentum, we expect the metasurface to experience a backaction as it thermally emits, raising interesting possibilities for future research.

Our results provide a step towards a generalized solution to custom wavefront generation in a compactified form factor advantageous for a number of applications. These devices do not need to be externally excited by a coherent source and may produce arbitrarily chiral responses despite being singly patterned. In conjunction with the prospect of custom wavefront generation, the wavelength-selective emission confers efficient use of thermal energy in comparison with blackbodies, which holds the promise for exciting opportunities in custom energy harvesting systems such as solar thermal electric generators, for compact custom sensors across the IR, and for thermally driven IR communications platforms. Beyond emission, our high-Q metasurfaces support intrinsically chiral responses associated with three-dimensional structures while being patterned as if they were two-dimensional, showing that such responses to not require multi-layer or obliquely etched structures[37]. By incorporating our design principles into lossless media, our results represent a platform for spatially tailoring arbitrarily chiral responses in a simplified manufacturing scheme, with applications including biological sensing, topological photonics and chiroptics.

Online content

Any methods, additional references, Nature Portfolio reporting summaries, source data, extended data, supplementary information, acknowledgements, peer review information; details of author contributions and competing interests; and statements of data and code availability are available at https://doi.org/10.1038/s41565-024-01763-6.

References

1. Wolf, E. *Introduction to the Theory of Coherence and Polarization of Light* (Cambridge Univ. Press, 2007).
2. Jung, D. et al. Next-generation mid-infrared sources. *J. Opt.* **19**, 123001 (2017).
3. Carminati, R. & Greffet, J.-J. Near-field effects in spatial coherence of thermal sources. *Phys. Rev. Lett.* **86**, 1660 (1999).
4. Greffet, J.-J. et al. Coherent emission of light by thermal sources. *Nature* **416**, 61–64 (2002).
5. Luo, C., Narayanaswamy, A., Chen, G. & Joannopoulos, J. D. Thermal radiation from photonic crystals: a direct calculation. *Phys. Rev. Lett.* **93**, 19–22 (2004).
6. Lee, B. J., Fu, C. J. & Zhang, Z. M. Coherent thermal emission from one-dimensional photonic crystals. *Appl. Phys. Lett.* **87**, 071904 (2005).
7. Dahan, N. et al. Enhanced coherency of thermal emission: beyond the limitation imposed by delocalized surface waves. *Phys. Rev. B* **76**, 045427 (2007).
8. Liu, X. et al. Taming the blackbody with infrared metamaterials as selective thermal emitters. *Phys. Rev. Lett.* **107**, 045901 (2011).
9. Costantini, D. et al. Plasmonic metasurface for directional and frequency-selective thermal emission. *Phys. Rev. Appl.* **4**, 14023 (2015).
10. Inampudi, S., Cheng, J., Salary, M. M. & Mosallaei, H. Unidirectional thermal radiation from a SiC metasurface. *J. Opt. Soc. Am. B* **35**, 39 (2018).
11. Duggan, R., Ra'di, Y. & Alù, A. Temporally and spatially coherent emission from thermal embedded eigenstates. *ACS Photonics* **6**, 2949–2956 (2019).
12. He, M. et al. Deterministic inverse design of Tamm plasmon thermal emitters with multi-resonant control. *Nat. Mater.* **20**, 1663–1669 (2021).
13. Caldwell, J. D. et al. Low-loss, infrared and terahertz nanophotonics using surface phonon polaritons. *Nanophotonics* **4**, 44–68 (2015).
14. Wang, T. et al. Phonon-polaritonic bowtie nanoantennas: controlling infrared thermal radiation at the nanoscale. *ACS Photonics* **4**, 1753–1760 (2017).
15. Yu, N. et al. Light propagation with phase discontinuities: generalized laws of reflection and refraction. *Science* **334**, 333 (2011).
16. Arbabi, A., Horie, Y., Bagheri, M. & Faraon, A. Dielectric metasurfaces for complete control of phase and polarization with subwavelength spatial resolution and high transmission. *Nat. Nanotechnol.* **10**, 937–944 (2015).
17. Manchon, A. et al. New perspectives for Rashba spin–orbit coupling. *Nat. Mater.* **14**, 871–882 (2015).
18. Parappurath, S. et al. Direct observation of topological edge states in silicon photonic crystals: spin, dispersion, and chiral routing. *Sci. Adv.* **6**, eaaw4137 (2020).
19. Lin, J. et al. Polarization-controlled tunable directional coupling of surface plasmon polaritons. *Science* **340**, 331–334 (2013).
20. Jisha, C. P. et al. Geometric phase in optics: from wavefront manipulation to waveguiding. *Laser Photonics Rev.* **15**, 2100003 (2021).
21. Dahan, N. et al. Geometric Doppler effect: spin-split dispersion of thermal radiation. *Phys. Rev. Lett.* **105**, 136402 (2010).
22. Rong, K. et al. Photonic Rashba effect from quantum emitters mediated by a berry-phase defective photonic crystal. *Nat. Nanotechnol.* **15**, 927–933 (2020).
23. Chen, Y. et al. Compact spin-valley-locked perovskite emission. *Nat. Mater.* **22**, 1065–1070 (2023).
24. Mahmud, M. S. et al. Chiral plasmonic metasurface absorbers in the mid-infrared wavelength range. *Opt. Lett.* **45**, 5372–5375 (2020).
25. Shen, Z. et al. Terahertz spin-selective perfect absorption enabled by quasi-bound states in the continuum. *Opt. Lett.* **47**, 505–508 (2022).
26. Wang, X. et al. Observation of nonvanishing optical helicity in thermal radiation from symmetry-broken metasurfaces. *Sci. Adv.* **9**, ade4203 (2023).
27. Nguyen, A. et al. Large circular dichroism in the emission from an incandescent metasurface. *Optica* **10**, 232–238 (2023).
28. Blanchard, C. et al. Metallo-dielectric metasurfaces from thermal emission with controlled spectral bandwidth and angular aperture. *Opt. Mater. Express* **12**, 443111 (2022).
29. Caloz, C. et al. Electromagnetic nonreciprocity. *Phys. Rev. Appl.* **10**, 047001 (2018).
30. Overvig, A. C., Mann, S. & Alù, A. Thermal metasurfaces: complete emission control by combining local and nonlocal light-matter interactions. *Phys. Rev. X* **11**, 021050 (2021).
31. Overvig, A. & Alù, A. Diffractive nonlocal metasurfaces. *Laser Photonics Rev.* **16**, 2100633 (2022).
32. Shastri, K. & Monticone, F. Nonlocal flat optics. *Nat. Photonics* **17**, 36–47 (2023).
33. Miller, D. A. B. Why optics needs thickness. *Science* **379**, 41–45 (2023).
34. Overvig, A. C. et al. Selection rules for quasibound states in the continuum. *Phys. Rev. B* **102**, 035434 (2020).
35. Overvig, A. C., Yu, N. & Alù, A. Chiral quasi-bound states in the continuum. *Phys. Rev. Lett.* **126**, 073001 (2021).

36. Overvig, A. C., Kasahara, Y., Xu, G. & Alù, A. Demonstration of a polarization-agnostic geometric phase in nonlocal metasurfaces. Preprint at https://arxiv.org/abs/2302.13215v1
37. Chen, Y. et al. Observation of intrinsic chiral bound states in the continuum. *Nature* **613**, 474–478 (2023).
38. Overvig, A. C., Mann, S. & Alù, A. Spatio-temporal coupled mode theory for nonlocal metasurfaces. *Light Sci. Appl.* **13**, 28 (2024).
39. Koshelev, K. et al. Asymmetric metasurfaces with high-*Q* resonances governed by bound states in the continuum. *Phys. Rev. Lett.* **121**, 193903 (2018).
40. Blanach, C., Viktorovitch, P. & Letartre, X. Perturbation approach for the control of the quality factor in photonic crystal membranes: applications to selective absorbers. *Phys. Rev. A* **90**, 033824 (2014).
41. Abujetas, D. R., van Hoof, N., ter Huurne, S., Rivas, J. G. & Sanchez-Gil, J. A. Spectral and temporal evidence of robust photonic bound states in the continuum on terahertz metasurfaces. *Optica* **6**, 996–1001 (2019).
42. Lu, G. et al. Engineering the spectral and spatial dispersion of thermal emission via polariton-phonon strong coupling. *Nano Lett.* **21**, 1831–1838 (2021).
43. Miller, D. A. B., Zhu, L. & Fan, S. Universal modal radiation laws for thermal emitters. *Proc. Natl Acad. Sci. USA* **114**, 4336–4341 (2017).
44. Mohtashami, Y. et al. Light-emitting metalenses and meta-axicons for focusing and beaming of spontaneous emission. *Nat. Commun.* **12**, 3591 (2021).
45. Iyer, P. P. et al. Unidirectional luminescence from InGaN/GaN quantum-well metasurfaces. *Nat. Photon.* **14**, 543–548 (2020).
46. Zhu, L. & Fan, S. Near-complete violation of detailed balance in thermal radiation. *Phys. Rev. B* **90**, 220301 (2014).

Publisher's note Springer Nature remains neutral with regard to jurisdictional claims in published maps and institutional affiliations.

Springer Nature or its licensor (e.g. a society or other partner) holds exclusive rights to this article under a publishing agreement with the author(s) or other rightsholder(s); author self-archiving of the accepted manuscript version of this article is solely governed by the terms of such publishing agreement and applicable law.

© The Author(s), under exclusive licence to Springer Nature Limited 2024

Methods

Materials

The thermal metasurfaces were fabricated using conventional semiconductor processing steps. To start, we used electron beam deposition to deposit 150 nm of Au and 40 nm of Al_2O_3 on top of an undoped, single-side-polished Si wafer. We then used plasma-enhanced chemical vapour deposition (CVD) to deposit 2,640 nm of SiO_2 and 1,460 nm of Si. We also deposited an individual layer of SiO_2 and a bilayer of Si on SiO_2 on Si substrates to extract the dielectric functions using IR-variable angle spectroscopic ellipsometry (IR-VASE, Woollam). The ellipsometric fits are displayed in Supplementary Fig. 1, and extracted dielectric functions of Si and SiO_2 can be found in Supplementary Fig. 2b,c, respectively. These dielectric functions were implemented into the numerical calculations. A schematic of the substrate is shown in Supplementary Fig. 2a.

The wafer was then diced into 1 cm × 1 cm pieces, which were spin-coated with polymethyl methacrylate (PMMA). A 10 nm Au charge compensation layer was then deposited on top of the PMMA using sputtering, and the samples were patterned using standard electron beam lithography. The samples were then developed using methyl isobutyl ketone, and 40 nm of Al_2O_3 was deposited on top as an etch mask. A lift-off procedure was then performed using Remover PG, and the substrates were etched using a fluorine-based inductively coupled plasma etcher (Oxford PlasmaPro System 100 Cobra).

Fabrication of the metasurfaces

We fabricate our metasurfaces using a standard process flow shown in Supplementary Fig. 3. First, e-beam deposition of a thin layer of gold is performed on top of a silicon wafer. Then, plasma-enhanced CVD of the thin films of oxide and silicon is carried out. We lithographically define the metasurface pattern in the silicon layer using e-beam lithography, wherein we use PMMA as a resist, a thin layer of sputtered gold as a discharge layer and methyl isobutyl ketone to develop the resist post exposure. A lift-off procedure transfers the pattern from PMMA to a thin layer of alumina: alumina is deposited by e-beam deposition and then Remove PG dissolves the PMMA and unwanted alumina. Finally, reactive ion etching transfers the pattern into the layer silicon.

Characterization of the metasurfaces

Absorption and thermal emission measurements were performed using a Bruker INVENIO-R FTIR coupled with a Hyperion microscope or in-house built angle-resolved thermal emission setup.

Poincaré mapping of the absorption (Fig. 3) was performed using a Hyperion microscope. A 15× Cassegrain objective (Newport numerical aperture 0.4) was used for the absorption measurements, which provides an azimuthal angle of incidence of $\theta \approx 22°$ for all radial angles ($\phi = 0 - 180°$). To achieve a pure polarization state for the incident light, we first restricted the radial angles to only allow for light to be incident along the x direction (Supplementary Fig. 4) using a three-dimensionally printed aperture. This technique has been employed in previous publications as a way of restricting to only one polarization state and tuning the measured angle of incidence[47]. Polarimetry was performed by placing a broadband mid-IR (2.5–7 µm, Bernhard Halle Nachfl., BHN 2016.0083.0000-K01) quarter waveplate (QWP) and CaF_2 wire grid polarizer (Thorlabs WP50H-C) in the beampath between the FTIR and the microscope. The extinction ratio of the CaF_2 wire grid polarizer (Thorlabs WP50H-C) is >150:1 at 3 µm and 300:1 at 8 µm.

To produce linear polarization states, the polarizer was placed in the polarizer slot of the microscope. The equator can then be mapped by changing the polarizer angle between 0° and 180°. Therefore, the S_1 axis of the Poincare sphere can be isolated at polarizer angles of 0° and 90° and the S_2 axis at polarizer angles of 45° and 135°. An alternate setup was required to produce CP polarization states, wherein the polarizer and QWP were placed in the beampath between the FTIR and the microscope as shown in Supplementary Fig. 2.

Angle-resolved thermal emission measurements (Figs. 3 and 5) were performed using a Linkam THMS600 heated stage mounted upright on a commercially available, motorized rotation stage (Thorlabs HDR50). The temperature stability of the Linkam THMS600 heating stage is reported to be <0.01 °C. Micrometre stages (Thorlabs PT1) are used to align the sample within the beam path. The sample was heated to 300 °C, and the emission was collimated using a 90° off-axis parabolic mirror and then directed into the FTIR. The broadband mid-IR QWP and CaF_2 wire grid polarizer (mentioned above) were placed between the mirror and the FTIR to determine the polarization state of the thermal emission. The beampath of the thermal emission setup, showing the placement of the QWP and polarizer, is provided in Supplementary Fig. 5. An array of vertically aligned carbon nanotubes (VACNT, 500-µm-tall on Si substrate, NanoLab) was used as a 'blackbody' reference sample in calculating the sample emissivity. At 500 µm tall, the emissivity of VACNT forests grown using the CVD has been reported to be 0.97–0.98 [2]. Further, the scattering properties of VACNT forests have been shown to be isotropic out to steep oblique incidence angles ($R \leq 0.1$ for $\theta < 60°$).

Error analysis in polarization-resolved thermal emission measurements

Sources of error in the polarization-resolved thermal emission measurements include the orientation of the polarizer, QWP and sample, which were all aligned manually. We estimate this alignment error to be ±2° for each component. The resultant uncertainty in the measured Stokes parameters can be estimated using the Mueller calculus. Here, the polarization of the emitted light is represented by the input Stokes vector S_{in} and the alignment of the sample can be represented by a rotation matrix M_{rot}. The linear polarizer and QWP are represented by the Mueller matrices M_p and M_q, respectively, with the misalignment of each component also being accounted for using rotation matrices. The output Stokes vector for the linear polarization measurements can then be calculated as

$$S_{out} = M_{rot,p} M_p M_{rot,s} S_{in},$$

where $M_{rot,p}$ and $M_{rot,s}$ are the rotation matrices for the polarizer and sample, respectively. Assuming an arbitrary input and that the polarizer is aligned horizontally ($\theta = 0°$ in the lab frame), the resultant Stokes vector can be calculated as

$$S_{out} = \begin{bmatrix} \frac{1}{2}(S_0 + S_1) \\ \frac{1}{2}\left((S_0 + S_1)\cos(2\theta_p + 2\theta_s)\right) \\ \frac{-1}{2}\left((S_0 + S_1)\sin(2\theta_p + 2\theta_s)\right) \\ 0 \end{bmatrix},$$

where θ_p and θ_s are counterclockwise rotation angles corresponding to the misalignment of the polarizer and sample, respectively. Now, the uncertainty in S_{out} can be calculated as

$$\Delta S_{out}^2 = \sum \left(\frac{\partial S_{out}}{\partial \theta_i}\right)^2 \Delta\theta_i^2,$$

where $\Delta\theta_i$ is the uncertainty in the orientation of the i component. Therefore, for the linear polarized measurement,

$$\Delta S_{out}^2 = \begin{bmatrix} 0 \\ (\Delta\theta_p^2 + \Delta\theta_s^2)\sin(2\theta_p + 2\theta_s)^2 (S_0 + S_1)^2 \\ (\Delta\theta_p^2 + \Delta\theta_s^2)\cos(2\theta_p + 2\theta_s)^2 (S_0 + S_1)^2 \\ 0 \end{bmatrix}.$$

Assuming $S_1 = S_0 = +1$ and $\Delta\theta_p = \Delta\theta_s = 2^\circ$, the uncertainty in $\Delta S_1 \approx \pm 0.02$. Note that, although this example was for the measurement of thermal emission with polarization $S_1 = +1$, by changing the polarizer angle this uncertainty value holds for other input linear polarizations (that is, $S_1 = -1$ or $S_2 = \pm 1$). Measuring chiral emission requires the addition of a QWP between the sample and the polarizer,

$$S_{out} = M_{rot,p} M_p M_{rot,q} M_q M_{rot,s} S_{in}.$$

Here the QWP is aligned at 45° with respect to the optical axis. From this expression, the output Stokes vector for an arbitrary input is

$$S_{out} = \begin{bmatrix} \frac{1}{2}(S_0 + S_3) \\ \frac{1}{2}\left((S_0 + S_3)\cos\left(2\theta_p + 2\theta_s + 2\theta_q\right)\right) \\ \frac{-1}{2}\left((S_0 + S_3)\sin\left(2\theta_p + 2\theta_s + 2\theta_q\right)\right) \\ 0 \end{bmatrix},$$

where θ_q represents the misalignment of the QWP. The uncertainty of the output Stokes vector can then be calculated as

$$\Delta S_{out}^2 = \begin{bmatrix} 0 \\ (\Delta\theta_p^2 + \Delta\theta_s^2 + \Delta\theta_q^2)\sin\left(2\theta_p + 2\theta_s + 2\theta_q\right)^2 (S_0 + S_3)^2 \\ (\Delta\theta_p^2 + \Delta\theta_s^2 + \Delta\theta_q^2)\cos\left(2\theta_p + 2\theta_s + 2\theta_q\right)^2 (S_0 + S_3)^2 \\ 0 \end{bmatrix}.$$

Assuming purely chiral emission ($S_3 = S_0 = +1$) and $\Delta\theta_p = \Delta\theta_s = \Delta\theta_q = 2^\circ$ the uncertainty in $S_1 \approx \pm 0.04$. Note that the input is S_3, whereas the output is S_1 due to the QWP.

Note that this error analysis considers the rotational misalignment of the optical components with respect to the optical axis. Another source of measurement error includes the alignment of the sample with respect to the focal point of the parabolic mirror. For the sample to be aligned, the focal point of the parabolic mirror and sample need to be at the centre of rotation of the rotation stage. In-plane misalignment can result in an asymmetric collection of signal as a function of angle and the dispersion not being correctly centred at $\theta = 0^\circ$. Out-of-plane misalignment can result in a reduction in the collected signal from the device (lower emissivity). Correctly aligning the sample requires that a lamp be placed in the beampath of the emission directed back towards the sample and observing the focal spot. First, the focal spot from the parabolic mirror is aligned to the centre of rotation of the rotation stage, then the sample is moved into the focal spot using a micrometre stage at the base of the heated stage. Then, the sample is rotated to a steep angle of incidence. If the focal spot stays in the same location on the sample, then the sample is aligned; if not, then the micrometre stages are used to further align the sample. Sources of error that lead to non-ideal performance of the device are the result of fabrication imperfections.

Data availability

All data are available in the main text or Supplementary Information.

References

47. Maß, T. W. W. & Taubner, T. Incident angle-tuning of infrared antenna array resonances for molecular sensing. *ACS Photonics* **2**, 1498–1504 (2015).

Acknowledgements

The authors thank S. Mann for helpful discussions. This work was supported by the Department of Defense Vannevar Bush Faculty Fellowship (A.A.) and the Air Force Office of Scientific Research MURI programme (A.A.). This work was performed in part at the Advanced Science Research Center NanoFabrication Facility of the Graduate Center at the City University of New York.

Author contributions

Conceptualization: A.C.O., J.R.N. and A.A. Methodology: J.R.N., A.C.O. and M.C. Investigation: J.R.N., A.C.O. and M.C. Visualization: A.C.O. Funding acquisition: A.A. Project administration: A.A. Supervision: A.A. Writing—original draft: A.C.O. Writing—review and editing: J.R.N., A.C.O., M.C. and A.A.

Competing interests

J.R.N., A.C.O. and A.A. authored US Patent App. 17/651,078 related to this work. M.C. declares no competing interests.

Additional information

Supplementary information The online version contains supplementary material available at https://doi.org/10.1038/s41565-024-01763-6.

Correspondence and requests for materials should be addressed to Andrea Alù.

Peer review information *Nature Nanotechnology* thanks Benjamin Vest for their contribution to the peer review of this work.

Reprints and permissions information is available at www.nature.com/reprints.